Available online at www.sciencedirect.com

jmr&t Journal of Materials Research and Technology

journal homepage: www.elsevier.com/locate/jmrt

Original Article

Effect of alloying elements on laser surface modification of powder metallurgy to improve surface mechanical properties of beta titanium alloys for biomedical application

M.C. Rossi [a,*], J.M. Amado [b], M.J. Tobar [b], A. Vicente [a], A. Yañez [b], V. Amigó [a]

[a] Instituto de Tecnología de Materiales, Universitat Politècnica de València, Valencia, Spain
[b] Departamento de Ingeniería Industrial II, Universidade da Coruña, Ferrol, Spain

ARTICLE INFO

Article history:
Received 29 March 2021
Accepted 8 July 2021
Available online 16 July 2021

Keywords:
Mechanical properties
Laser melting
Microstructure
Martensite
Ti–35Nb–10Ta
Ti–30Nb–4Sn

ABSTRACT

Beta-type titanium alloy surfaces (Ti–35Nb–10Ta (TNT) and Ti–30Nb–4Sn (TNS)) were modified by laser using a power of 1000 W and speed of 6.7 mm/s (Condition A) and a power of 1500 W with speed of 10 mm/s (Condition B). Increasing laser conditions, the thickness of the molten layer was also increased. The initial equiaxed grains changes to quite elongated grains shape. The surfaces were structured under α″ martensite, α and matrix β. The β phase content decreased slightly and the α″ phase increased for both alloys increasing the laser conditions. The condition A increased the elastic modulus (E) and decreased the hardness while condition B did not affect the mechanical properties surface for the TNT system compared to base metal (BM). In TNS system the laser condition A decreased the E and increased the hardness while increasing the laser parameters (Condition B) both E and hardness decreased compared to BM. The laser surface treatment was influenced by the levels of alloying elements present promoting most significant changes in the microstructure and mechanical properties in the TNS system.

1. Introduction

In the development of new titanium alloys for biomedical applications, it is of great interest to achieve a lower elastic modulus. Such reduction improves osseointegration and avoids bone atrophy by preventing stress-shielding and bone resorption [1]. β-Type Ti alloys [2] show the most promising properties in this respect, yielding also improved strength and corrosion resistance with respect to their α and α+β microstructure. They are produced by the addition of β-stabilizing elements that retain the β-phase when the metal is cooled rapidly from the β-*transus* temperature. A large number of alloying elements can be used as β-stabilizers, being refractory elements as Nb, Mo or V those used in a more significant amount. Additions of other elements (Ta, Zr, Sn) are used to create many ternary or quaternary combinations and

* Corresponding author.
E-mail address: mrncorrea90@gmail.com (M.C. Rossi).
https://doi.org/10.1016/j.jmrt.2021.07.037

further tune the properties of the resulting material. According to Niinomi [3] who revised the mechanical properties of this type of alloys. Among them, much attention has been paid to those based on the Ti–Nb system, in virtue of its good biocompatibility, low elastic modulus and shape memory characteristics. In the work of Tane et al., 2016, the difference in the elastic modulus of the β Ti–Nb–Zr–Ta alloy during aging at room temperature [4] was investigated. Other authors have studied the addition of Fe in the Ti–35Nb–10Ta alloy and β-type Ti–35Nb–7Zr–6Ta in order to improve the diffusion process that can be hampered by the presence of refractory elements [5,6]. Other authors have studied the microstructure and the deformation mechanisms by load and unloading mechanisms of the Ti–Nb–Ta–Zr alloy for biomedical application [7].

The incorporation to titanium of a significant number of refractory elements as mentioned above, as Ta, Mo, or Nb is complicated and expensive using conventional techniques. Powder metallurgy (PM) can represent an alternative in the development of these alloys. It is known its capability to obtain near-net shape components of new materials that are not accessible by other routes [8], particularly when the elemental material composition is significantly reactive, refractory or present difficulties to atomic diffusion. A wide variety of beta-Ti–Nb alloys have already been processed by PM techniques which fulfill the requirements in terms of material performance [4,9]. However, these technologies are accompanied by an inherent open porosity in the processed components, which can impair its surface properties in terms of corrosion and fatigue resistance. This porosity can be closed, at least in part, by parameter calibration, but it is common to use surface modification technologies that can, in addition close the pores on the surface and confer specific properties [10]. These surface modification methods can be classified into mechanical such as grinding or blasting, chemical such as acid etching or anodic oxidation, and physical methods such as thermal projection coating processes. [11,12], mainly by atmospheric plasma, Physical Vapor Deposition, Ion implantation or glove discharge plasma treatment [13]. However, in recent years, the application of lasers as a surface modification technique has acquired a predominant role, both as surface thermal treatment [14], texturing of alloy surface to femtosecond laser [15], production of specific alloys [16,17], or by coating through direct powder deposition (laser cladding) [18,19] to obtain from bioactive to bio-inert coatings. Most of these surface modification techniques are done by heat transfer from the laser-substrate system (metal surface). The energy transfer performed by the laser can be investigated by studying the physical parameters of the laser, such as energy, speed and power [20]. These parameters influence the quality of heat transfer, which also depends on the region being treated, due to the oscillatory nature of the waves [21]. In order to reduce the energy loss of a dynamic system, the entropy of a system, which measures the magnitude of the energy is a studied parameter [22]. Vilar and Almeida [23] exposes different techniques of superficial modification by laser, including superficial melting. The laser surface melting (LSM) process, or laser re-melting according to Zhang et al. [24], consists in scanning the surface of the material with a high-power and defocused laser beam to produce the rapid melting and solidification of a thin layer. A dense re-melted material is obtained whose thickness may be controlled by the laser parameters. The fusion process not only allows to eliminate surface porosity, adjusting the physical parameters in order to control the heat transfer [25], but also provides with a better diffusion of the most refractory elements in PM parts. In addition, it produces metallurgical variations in the treated material. Under melting and fast cooling rates, the microstructure and phase composition of the surface is frequently modified to provide with better mechanical or chemical characteristics, as in works using Ti–12Mo–6Zr–2Fe, Mg–Zn–Dy, Ti–Al–Zr–Mo alloys in which the surface treatment of these materials improved corrosion resistance [26], increased wettability [27], with microstructural transformations [28] which also influence mechanical properties. Beta Ti alloys are commonly classified in terms of the weight percentage of β stabilizer. The molybdenum equivalent Mo_{eq} is usually accepted as a normalizing parameter to describe the stability of the β (bcc) phase [2]. Alloys with Mo_{eq} ranging between 5% and 10% are called near β while between 10% and 30% are called metastable β. Both are metastable and hence heat treatable and hardenable. Upon quenching from high temperature or by mechanical deformation, martensitic (α′, α″) and other non-equilibrium phases (ω) can form which modify the mechanical properties of the alloy. In recent years it has been reported that increased α″ martensite contents could reduce the Young's modulus of these alloys. Reductions up to ~40 GPa, close to that of cortical bone, are obtained by cold-rolling or other deformation process [29–32]. Following these results, the characteristics of metallurgical transformations due to thermal processing and its effects on mechanical properties has also been investigated [33,34], in particular by LSM, in Ti–35Nb–2Ta–3Zr [35], Ti–30Nb–4Sn [36,37]and Ti–30Nb–2Sn [38]. In general, lowering effects in the value of the elastic modulus has been obtained although it is not clear how they are affected by the particular alloy type and the parameters of the treatment. This work evaluates the microstructural changes and mechanical properties obtained during the surface modification by laser of two β-Ti alloys: a near β, with composition Ti–30Nb–4Sn (TNS) and a metastable β with composition Ti–35Nb–10Ta (TNT). The main objective of this work was to improve the properties of surfaces of metallic alloys that are studied for biomedical application. The main drawbacks of biomaterials are the high elastic modulus and also the microporosity formation on the surface during the sintering process. The formed micropores can reduce the load-bearing cross section and consequently decrease the compressive strength of the samples. Laser treatment can help to improve the surface conditions of these materials produced by powder metallurgy. Due to powder metallurgy, the microporosity formed is difficult to eliminate completely. However, as it is a technique that has excellent advantages in the production of materials for orthopedic application, such as the use of temperatures below the melting point of the alloy elements, low production cost, and the production of a high number of samples in a short period of time, it is still widely used. Surface treatments can be a viable option in order to make these materials more applicable, by the quick melting–solidification of the surface. In the

design of prostheses, aspects that must be considered are: adequate mechanical properties, use of materials that do not change with time (wear-resistant) and compatible production cost. The laser treatment was performed with two different parameter configurations, applying the same specific energy at different scanning speeds so to assess the effect of the variation of the cooling rate (determined by the scan speed) on the final results.

2. Materials and methods

TNT and TNS samples were manufactured by the press-and-sinter powder metallurgy process. Elemental powders of titanium (99.7% purity; size d (0.5) = 29 μm), niobium (99.9%; 16 μm), tantalum (99.9%; 4.3 μm) and tin (99.8%; 44 μm) were used as precursor materials. Powders were weighed according to the nominal composition of the alloys, i.e., Ti–35Nb–10Ta (wt.%) and Ti–30Nb–4Sn (wt.%). Then they were mixed by an Inversina 2LTM turbine from Biocomponents, for one hour. After mixing, they were compacted in an INSTRON 1343 hydraulic press at 600 MPa, using a 30 × 12 mm floating die to obtain a thickness around 5 mm. The specimens in green were sintered in a high vacuum furnace (<10^{-4} mbar) Carbolite HVT 15/75/450, at a heating rate of 10 °C/min, up to 1250 °C. After a dwell time of 3 h, they were cooled into the furnace.

The LSM process was carried out by a Nd: YAG Rofin-Sinar laser pumped by DY-022 diodes, with maximum power 2200 W guided by optical fiber and mounted on a 6-axis ABB robotic arm, controlled by customized software that allows movement according to the trajectories scheduled. The laser beam was defocused in order to obtain a beam diameter d = 2 mm on the work surface. The laser was run in continuous mode and λ = 1064 nm was used to fuse the surface. Helium was used as a shielding gas at a flow rate of 20 L/min. The LSM used in this work is outlined in Fig. 1. Two sets of processing parameters, namely laser power P and scan speed v, were applied which are listed in Table 1 and labeled as condition A and B.

The parameter values were adjusted to give the same specific energy input E per unit surface but at different scanning speeds v. Specific energy, E, was defined by equation (1).

Table 1 – Test parameters used in the LSM process.

Treatment condition	Laser power P (W)	Scan speed v (mm/s)	Specific energy E (J/mm^2)
A	1000	6.67	75
B	1500	10	75

$$E = \frac{P}{d \cdot v} \quad (1)$$

A semi-analytical approach [39] was used to estimate the thermal cycles at the material due to the different parameter settings, as depicted in Fig. 1b). For the calculation, custom user routines were programmed in Matlab platform. A laser absorptivity of 30% into the material was assumed.

Remelted surface areas about 25 × 10 mm^2 were obtained on each sample (see in Fig. 2) by performing successive laser scans with a 1 mm distance (corresponding to a 50% overlapping ratio).

Microstructure characterization was performed by Optical Microscopy (OM) and Field Emission Scanning Electron Microscopy (FE-SEM). A Nikon Eclipse LV100 microscope was used to evaluate the general microstructural features of the processed samples. Phase and elemental composition were analyzed with an Auriga Compact microscope from Zeiss, equipped with X-ray dispersive energy detector (EDS) and Diffraction of Backscattered Electrons (EBSD) from Oxford Instruments Ltda. For the EBSD analysis, cross sections of the samples have been prepared according to standard metallographic techniques with a final polish, prior to analysis, for approximately 5 h with non-dried OPS solution in a vibratory polisher, to remove the surface layer deformed by cutting and metallographic preparation. The EBSD has been carried out in an Aztec HKL Max System, under an acceleration voltage of 20 kV with a step size of 450 nm, selecting the three possible phases to be analyzed, β-Ti, α-Ti and α″-martensite. The coordinate axes of the molten layer are shown in Fig. 1, with the X axis in the transverse direction of the beads, the Y axis in the direction of the laser and the Z axis perpendicular to the sample surface, being the study plane of the XZ. The patterns were analyzed using the Channel 5 software, after a 7% refinement of the EBSD data to reduce the non-indexed points,

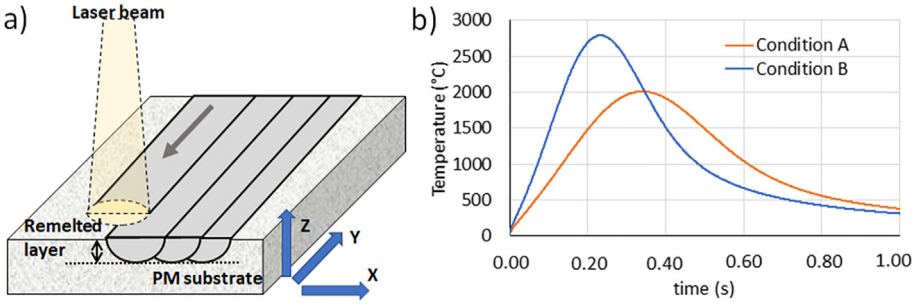

Fig. 1 – Scheme of the surface modification of the beta-type alloys used. a) Interaction of the laser beam with the surface of the sintered sample, modifying the texture pattern. b) Thermal cycles obtained by solving a heat conduction equation assuming a gaussian beam traveling on a semi-infinite media. This media was described with pure titanium properties. Based on these graphs cooling rates are in the range of 10^3 °C/s being larger at higher scan speeds and becoming similar as the material cools down.

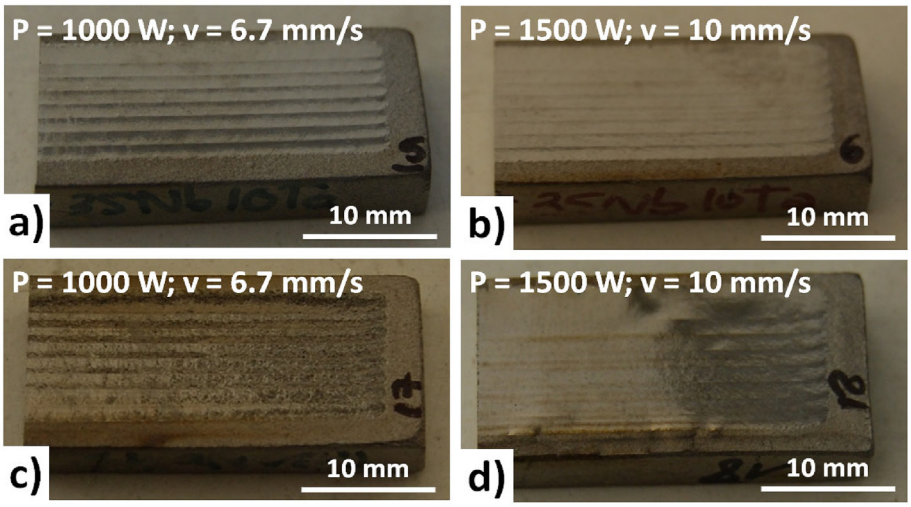

Fig. 2 – LSM at different test conditions. TNT: a) Condition A and b) Condition B; TNS: c) Condition A and d) Condition B.

obtaining a final indexing around 92% in the different samples. The grain detection angle to define the grains has been 10°. X-ray diffraction (XRD) was carried out in a Bruker D2PHASER equipment using 30 kV and 15 mA (30° to 90° (2θ) in 0.05° steps every 10 s).

Mechanical properties were obtained by nanoindentation tests, with an Agilent Nano G200 nanoindentator. Data was collected by the Continuous Stiffness Measurement (CSM) method with a Berkovich point, and was made an average of the values between 400 and 800 nm. A Poisson's coefficient of 0.3811 was applied to obtain the elastic modulus and hardness after the LSM. Indentations have been done at different regions of the material, both at the melted and the heat affected areas.

3. Results and discussion

3.1. *Microstructure*

Fig. 3 shows cross sectional views, perpendicular to laser scanning direction, of the LSM processed samples. The general features of the original sintered material are seen at the upper part of each image. Under backscattered electron (BSE) inspection, porosity (95.7% relative density) is visible in all samples together with brighter regions which are related to a higher content of heavier elements and were identified as niobium. Many Nb particles remain un-melted after the sintering process and those melted diffuse locally yielding enriched Nb regions.

Their presence is more significant in the TNT samples likely due to its higher Nb weight ratio as compared to the TNS alloy. Un-melted tantalum particles in the TNT samples are hardly detected, probably due to the smaller size of the Ta powder as with respect to the Nb, thus easing the fusion process. One of the causes that disadvantages and makes particle fusion difficult is its size. Larger particles can reduce laser penetration [40]. A proportion of the laser beam, during the surface treatment process, is reflected from the upper surface of the material layer. This phenomenon leads to insufficient absorption of thermal energy in the area of action. In this way, the heat generated is insufficient to melt particles of the powder, which during the sintering process was not possible. However, the purpose of the surface treatment was not to melt the samples, but only improve the surface conditions, like closing the open pores. The melting layer after the LSM process is visible at the bottom of the images where the overlapping of successive melting pools is clearly distinguished. After laser melting, and independently of the test conditions, the material appears fully dense, free of porosity or undissolved particles, with a more homogeneous elemental distribution. An effective melting depth for the LSM layer was

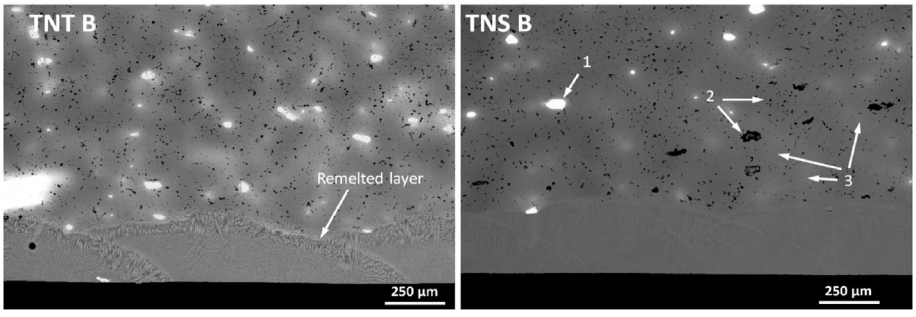

Fig. 3 – Cross-sectional view by FE-SEM (BSE) of sintered and LSM under condition B. 1: un-melted Nb particles located in sintered zone; 2: pores located in sintered zone; 3: enriched Nb regions located in sintered zone.

Table 2 – LSM mean melted depth, under different conditions tested.

	TNT-A	TNS-A	TNT-B	TNS-B
Mean depth (μm)	118 ± 53	186 ± 34	213 ± 31	191 ± 68

defined by averaging the maximum and minimum thickness values as measured on the images. Results are listed in Table 2 where the errors just denote the half difference between the two values. Depth differences arise in terms of sample material and testing condition: the depth of the melting layer is higher in the TNS than in the TNT samples and appears to increase with the scanning speed of the laser treatment. Assuming the same laser absorptivity for the two materials (there may be minor differences due to surface roughness or elemental composition) the reduced melting efficiency of the TNT samples could be explained by its higher content on refractory elements, which require a greater energy to reach their melting temperature (2080 °C in TNT alloy [41] and 1810 °C in TNS alloy [42]). To understand the effect of the test condition, it should be recalled that the laser energy absorbed at the surface is partially employed in rising the temperature of the material (eventually leading to melting) and partially dissipated by heat conduction to the bulk of the sample (despite the low thermal conductivity of titanium alloys, around 7 W/(m·K)). On laser scanning, heat dissipation diminishes on increasing the scan speed, as less interaction time is available for conduction. Heat energy is therefore more effectively employed in rising the temperature of the material, leading to larger melt pool size and hence, a deeper melting layer.

Fig. 4 displays a closer view to the material microstructure after LSM, which presents three distinct regions: the heat affected zone (HAZ), a narrow area along the melt pool solid–liquid interface (FL) corresponding to the mushy zone and, finally, the region of molted material within the melt pool, the fusion zone (FZ). The characteristic dendritic pattern associated to the high cooling rates imposed by laser melting process is visible, with dendrites growing in the direction of heat transfer.

The microstructure changes from columnar to columnar dendritic and equiaxed dendritic from the FL interface to the center of the FZ. This feature has extensively been studied [43,44] and is caused by differences in the thermal gradient G and the growth rate V of the solid–liquid interface at different locations of the solidification front created by the moving laser heat source. The FL represent the region with the highest thermal gradients and higher G/V ratio, resulting in columnar grains. The FZ correspond to points with higher solidification rates and lower G/V ratios, giving equiaxed dendrites. FL appears thicker for the TNS than for the TNT alloy, 125 ± 10 μm and 70 ± 20 μm respectively as measured on the image. As the

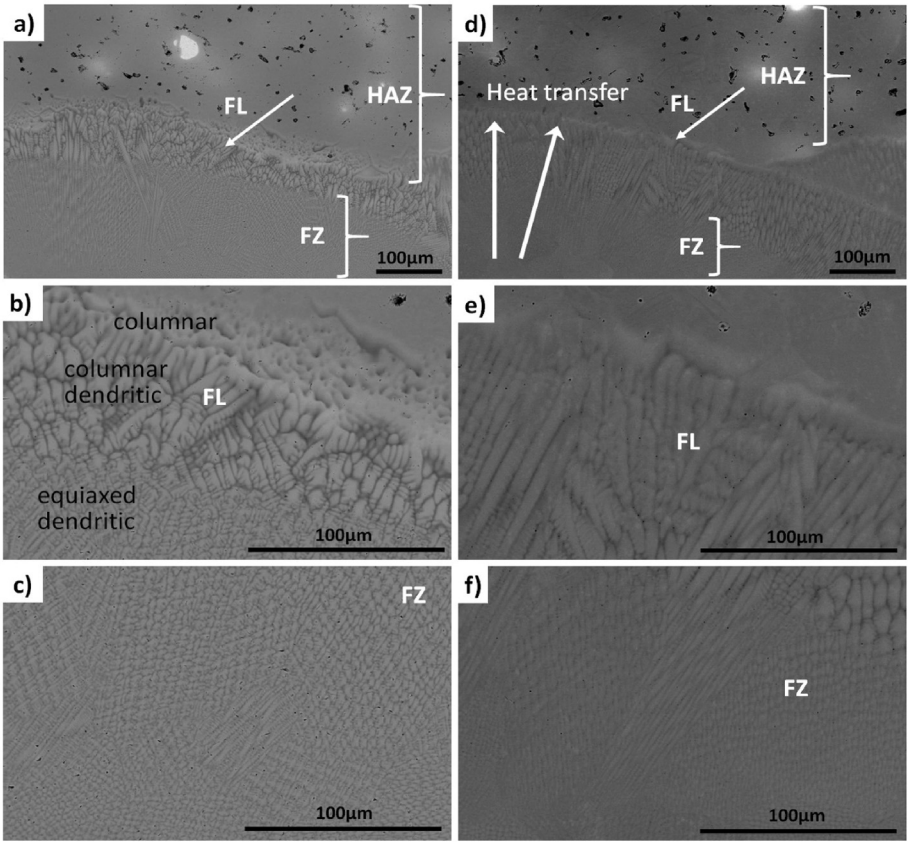

Fig. 4 – LSM microstructure of TNT under condition B a) indicated the thermally affected zone (HAZ), fusion zone (FZ) and fusion line (FL) indicating the re-melted zone by the arrow b) FL region details, c) details of the dendritic region located in FZ. TNS under condition B d) indicated the thermally affected zone (HAZ) fusion zone (FZ), and fusion line (FL) indicated by the arrow and the heat transfer region indicated by the arrows e) FL region details, f) FZ details of the dendritic region located in FZ. All samples were studied under FE-SEM inspection.

thickness of the mushy zone on solidification is mainly determined by the melting range and local thermal gradients [37], this seems a result of the different effect of the alloying elements on the base Ti metal thermal properties.

An example of the EDS elemental maps obtained for the TNT and TNS alloys after LSM is presented in Figs. 5 and 6. Aside from the presence of small un-dissolved particles, all the samples analyzed display a rather uniform distribution of the alloying elements. However, a clear dendritic pattern is perceptible, indicating micro-segregation phenomena during solidification. Inspection of the images reveals an enrichment of refractory elements Nb and Ta at the dendrites, while the interdendritic space becomes Nb and Ta depleted and enriched in Ti. This type of micro-segregation issues are common to many alloys under fast solidification which, specifically in the case of Ti alloys, have already been described in detail [45,46]. It can be understood in terms of the diffusion ability of the element and the local cooling rate. Upon solid precipitation and

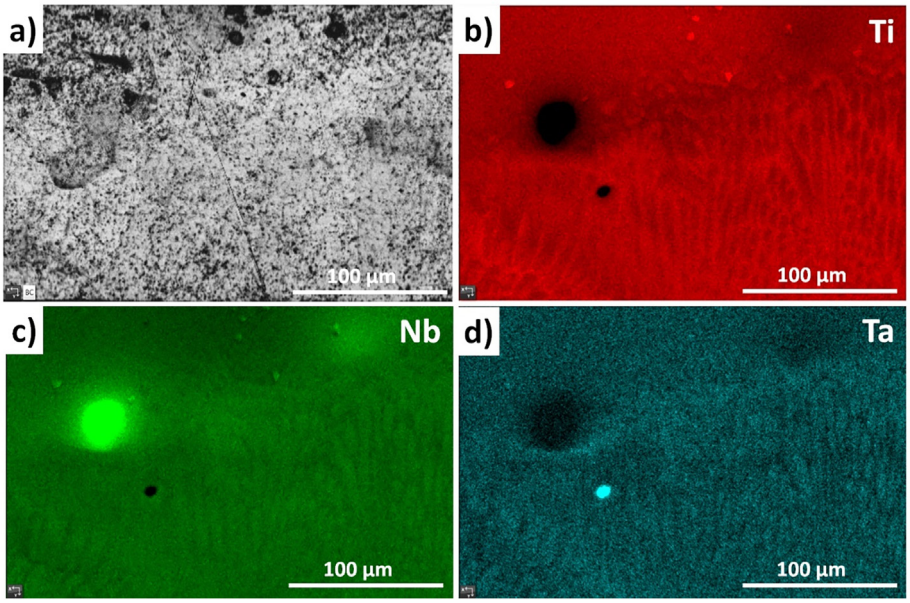

Fig. 5 – Elemental distribution maps for sample TNT processed under condition A. a) image of band contrast by EBSD. b), c) and d) distribution map of the elements Ti, Nb and Ta. Un-dissolved Nb and Ta particles can be clearly distinguished between the HAZ and FZ at c) and d) respectively.

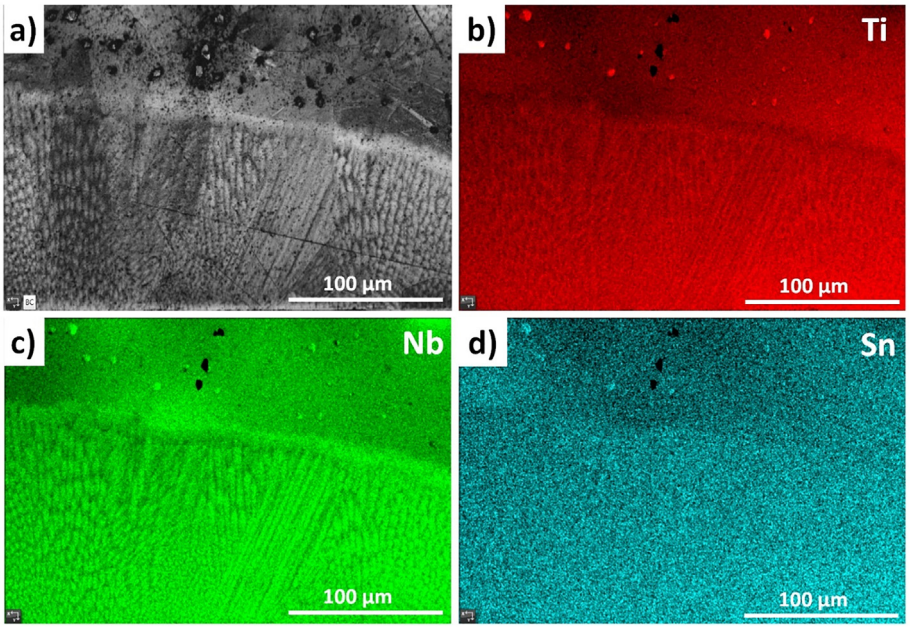

Fig. 6 – Elemental distribution maps for sample TNS processed under condition A. a) image of band contrast by EBSD. b), c) and d) distribution map of the elements Ti, Nb and Sn.

growth of the primary β phase, β formers as Nb and Ta become retained leading to the solute segregation in the interdendritic region. The low extent for diffusion of these element and the action of high cooling rates prevent their migration and solidification as in equilibrium conditions. Other elements show a more neutral behavior in virtue of their higher mobility within the β-matrix and do not promote segregation effects. This is the case for Sn which, as shown in Fig. 5, appears uniformly distributed without dendrite–interdendrite inhomogeneities.

The grain morphology after LSM processing can be examined in Fig. 7, where EBSD images of TNS and TNT samples and their corresponding Euler orientation maps are displayed. The initial equiaxed grain shape of the as-sintered microstructure (partially visible in the HAZ) changes to quite elongated grains in the FZ zone. Elongation nearly spans the whole melt layer thickness, and has the direction of the heat transfer, this is, perpendicular to the boundary of the melt pool in the direction of the thermal gradient. Grains are continuous over this boundary, indicating an epitaxial growth on solidification of the molten material. This means that atoms in melt pool accommodate to the preexisting lattices in the adjacent solid phase rather than arranging around nucleation sites. As a consequence of the epitaxial growth, the size and crystallographic orientation of the grains at the FZ are determined by those of the HAZ grains. Some noise is visible in both orientation maps, particularly in the TNS sample, with many unindexed points. This could be an indication of deformation or the presence of small microstructural transformation or secondary phases. Unindexed black pixels in the HAZ correspond to porosity in the as sintered materials.

3.2. *Phase composition*

XRD diffraction patterns in Fig. 8 shown the predominance of β phase formation for both TNT and TNS after the sintering process. The presence of α phase is also detected in the two materials, with a higher intensity in the TNS case. By the quantitative analysis, β/α percentages of 98.3/1.7 and 76.7/23.3 were obtained for the TNT and TNS respectively, revealing the near β character of the TNS alloy and too much higher extent of the TNT, which actually could be considered as β. These results confirm a sintered microstructure composed of β grains with α platelet precipitates, as described in previous works [5,38]. After LSM processing, the α signal appears largely suppressed in both samples and evidence of α″ is obtained in the TNS diffractogram, more obvious in condition B. It implies a clear metallurgical transformation after the laser treatment, whereby the material was heated above the β-*transus* and formed the α″ orthorhombic metastable phase upon cooling. The fraction of retained martensite seems to be influenced by the cooling rate of the process, in view of the more intense α″ peaks at larger scanning speed (condition B). By contrast, no evidence of martensitic transformation, in any of the laser treatment conditions, is found for the TNT sample, as no distinct α″ related peak can be identified. Anyway, it could be hindered by the intensity of the β signal if the amount of transformed martensite is low. An interesting feature of the XRD inspection is that, while the sintering samples display standard β peak intensity ratios, the LSM processed ones show a significant intensified peak related to the (200_β) plane. This indicates some kind of texturing in the treated material, with a preferred crystallographic orientation. Deformation, after rolling process for example, has been established as the reason for this texturing in β-Ti alloys [47]. But probably it is the strong growth of β grains in the direction of the thermal gradients what is behind this effect, as often seen in other processes involving laser melting [35,48].

A more clarifying picture of phase composition and distribution is obtained by means of EBSD phase maps presented in Fig. 9. It is seen that the β phase (in red) dominates the composition of TNT samples while the presence of α″ martensite (in green) is extensive in the TNS ones. The maps

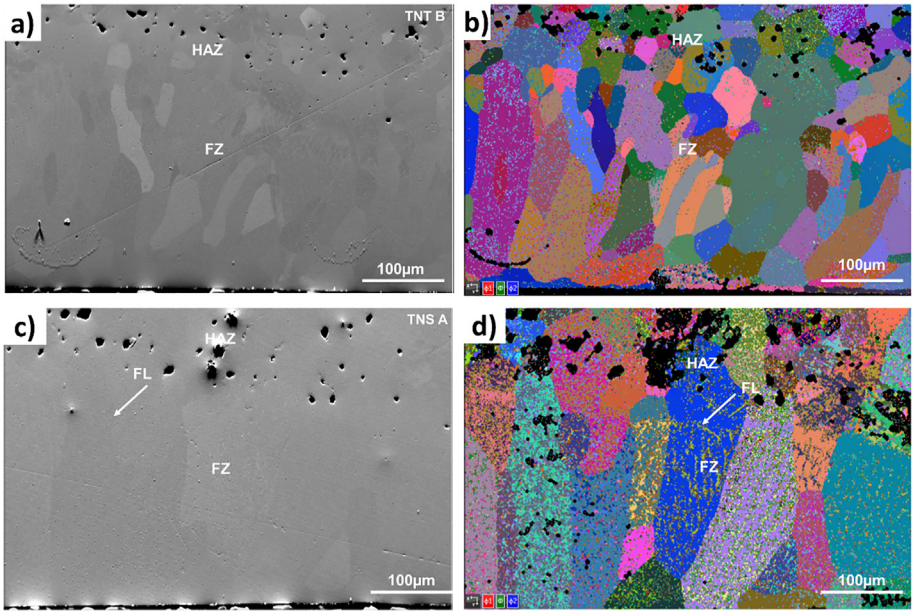

Fig. 7 – BSD (left) a), c) and EBSD euler image (right) b), d) of the TNT (up) and TNS (down) samples.

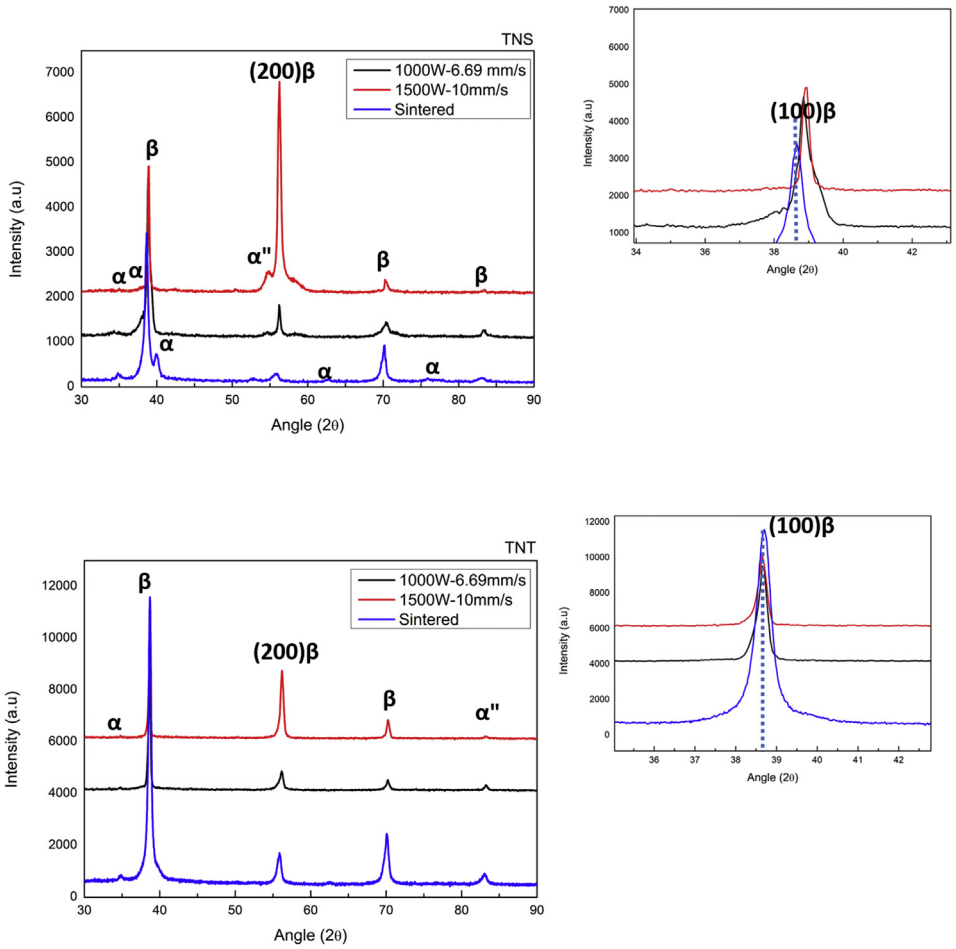

Fig. 8 – XRD profile of TNT (up) and TNS (down) samples as-sintered (blue curve) and after LSM (red and black curves) processing. The peak detail referring to the (100) plane of bcc structure, located at 2 theta = 38° is indicated in the upper right corner of each XRD pattern.

span over the FZ and the HAZ region, and the presence of the stable α phase (in blue) is hardly detected, thus confirming its suppression after the LSM process. The volume fractions measured in the maps are listed in Table 3.

The large faction of un-indexed pixels does not permit a rigorous quantification of the phases; however, it may be derived that the amount of α″ martensite in TNS nearly triples that of TNT. The change in laser scanning speed seems to have a modest effect on the metallurgical transformation as the α″ ratio increases in about 5% from condition A to B in both materials. Corresponding Image Pole Figure in its direction Z (IPF-Z) maps are shown at the left of each image, by which variations in the rate of martensitic transformation of prior β grains can be noticed. Some show an almost complete martensitic transformation while others are only partially transformed.

As noted in the introduction, quenching of the β phase from elevated temperatures can in result in diffuseless precipitation of different metastable phases. Martensitic α′ (hexagonal), α″ (orthorhombic) and ω phase (hexagonal) can be observed in ratios which mainly depend on the cooling rate and the amount of β stabilizers of the alloy. α′ transformation shifts to α″ and ω precipitation with increasing the β alloying elements [2]. As β stabilizers are added, the martensite start (Ms) temperature decreases between 380 K [49] and 423 K [50] and therefore the chance for martensite formation. As the critical concentration for full retention of the β phase is reached, α″ and ω phase precipitation become competitive process, being α″ promoted at high cooling rates. In Ti–Nb alloys α′ martensite is typically found below 15% Nb content, α″ is predominant between 15% and 25% and ω may be observed up to 35%, above which the β phase is completely retained [51]. Similarly, in Ti–Mo alloys α″ is predominant above 4% Mo while above 10% Mo the structure is completely retained β [52]. Our results verify such observations. The amount of β phase stabilizers in the TNT alloy (Nb,Ta) result in a Mo equivalent of 12 while in TNS the reduced Nb content and the neutral contribution of Sn count to a Mo equivalent of 7. So, a higher rate of martensite transformation could be predicted for TNS as to TNT after the LSM treatment. Similar results were obtained on water quenched Ti–Fe–Ta alloys at different Ta additions [53]. However, the resulting α″ contents seem somewhat higher than expected based on the β alloying percentages mentioned above, which were evaluated in

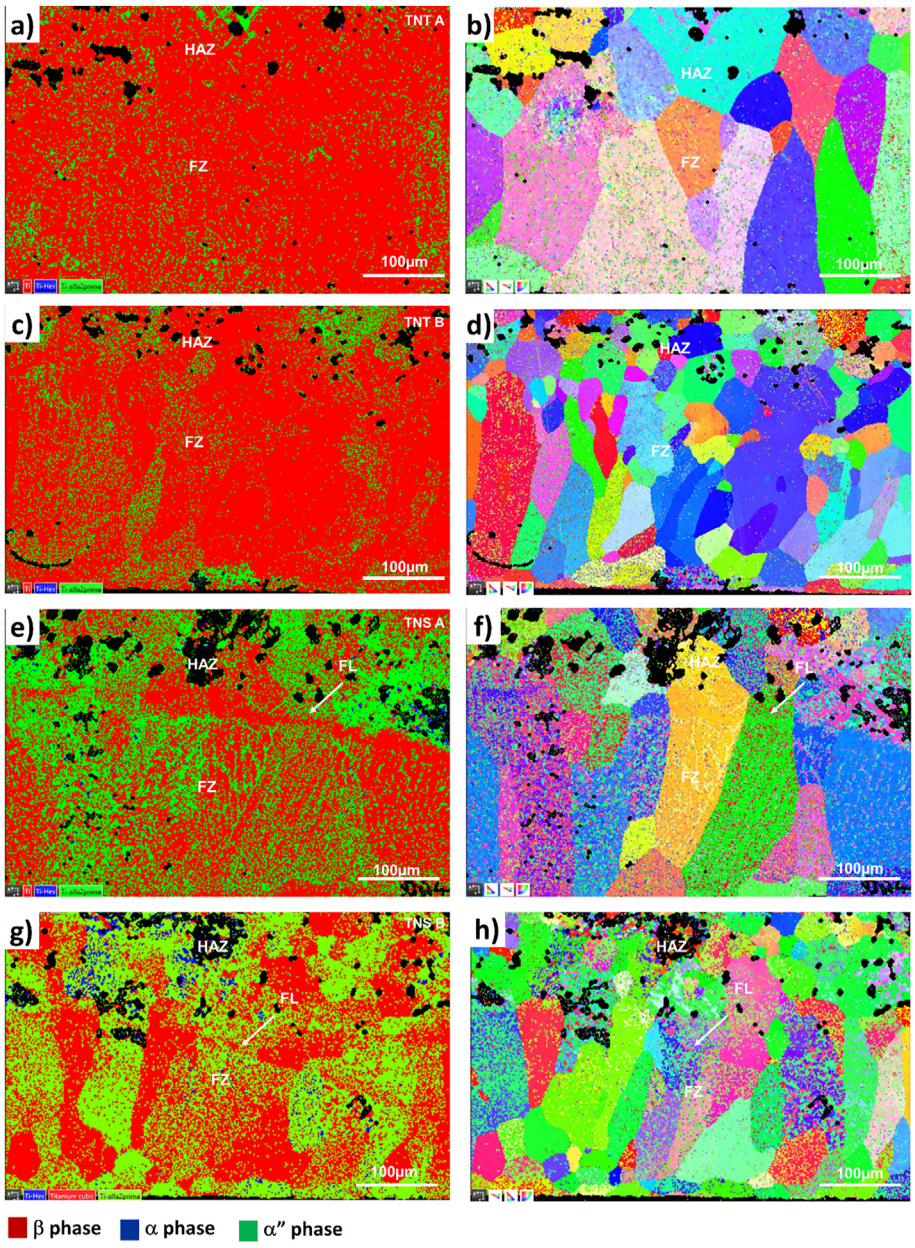

Fig. 9 – EBSD phase analysis of LSM processed samples. a), c), e) and g) EBSD phase images and b), d), f) and h) corresponding IPF-Z maps.

Table 3 – Phase composition obtained under different laser conditions. *By XRD **By EBSD volume fraction analysis. For the HAZ by LSM were obtained by XRD. It should be considered that in addition to the FZ, a part of the base material that presents an important transformation to the α″ phase has also been analyzed.

	As-sintered*		LSM**			
			Condition A		Condition B	
	TNT	TNS	TNT	TNS	TNT	TNS
β phase	98.3	76.7	72.90	40.49	73.04	38.51
α phase	1.7	23.3	0.22	0.98	0.23	2.02
α″ phase	–	–	13.86	33.20	16.49	40.45
Zero solutions			13.02	25.34	10.24	19.01

conventional air and water quenching process. Possibly, the higher cooling rates associated to laser treatments, in the range 10^3 K s^{-1} to 10^5 K s^{-1} [23], may have strengthen the diffuseless transformation. Furthermore, they must have suppressed ω phase precipitation in favor of α″. Though not detected in this study possibly due to limitations of the applied techniques, ω precipitation seems to be residual compared to α″. Several studies point to the attenuation of ω phase precipitation with increasing cooling rate and β stabilizers [54,55]. Finally, the role of interstitial elements (O, N, C and H) should also be considered. A higher fraction of martensite transformation is observed in Ti–Nb alloys at higher interstitial elements content [51], apparently due to the stabilizing the metastable α″ phase. The preexistent porosity of the LSM samples could rise the amount of dissolved oxygen

into the melt pool and thus have an important effect in the range of martensitic transformations.

The laser-fused zone was characterized by the presence of β columnar grains formed in both treatment conditions (Condition A and B) and in both TNS and TNT systems. It is noted that with the increase in the laser power and speed (Condition B), the systems presented grains less homogeneous and more elongated. It is clear that the morphology of the grains present in the FZ is affected by the heat flow during the rapid solidification process. The growth of β grains occurred in the FL region, close to HAZ, and clearly shows the influence of the laser condition applied to the increase of grain growth. In the condition of less power and less speed laser (condition A), the grains are larger and less elongated, regardless of the system. As the laser flow and power increase (Condition B), the grains become more elongated and smaller. This change in the sizes and morphology of β grains with the increase in laser conditions was more evident in the TNT system. Note that in FZ, the grains are smaller compared to the TNS system in condition B. This may be related to the amount of β-stabilizer elements contained in the TNT system. Columnar type grains were created towards the maximum temperature gradient. This microstructural change in regions close to HAZ, where high cooling rates occur, due to energy input, may have produced a transformation from β to the α'' phase, corroborating with the data found in the diffraction pattern.

3.3. *Mechanical properties*

Curves for nanoindentation tests of LSM materials are displayed in Figs. 9 and 10. The nanoindentation has been carried out by the continuous Stiffness method that gives a value of the hardness and elastic modulus at different depths. In this way it is possible to determine thin layers and the strength of small grains. As can be seen in Figs. 10 and 11, for the Ti–Nb–Ta alloy, the modulus hardly shows any variation for the two conditions analyzed. The hardness if greater, at any depth, in condition A. This equilibrium can therefore be determined for depths between 300 nm and 700–800 nm, which can be considered as the intrinsic properties of the material and independent of the surface preparation carried out and necessary to carry out the test. However, in the Ti–Nb–Sn alloy, and despite the fact that the behavior in the first nanometers is very different, the values tend to stabilize after 400 nm. Therefore, and considering the indicated measurement ranges, we obtain Table 4 with the values compared for the sintered material and with the laser surface treatment in the two conditions tested. Both hardness H and elastic modulus E show two different stages along the penetration depth of the tip. Measurements evolve in the first 200 nm until stable values are obtained up to 800 nm. Softening and hardening effects at small penetration depths are often encountered and attributed to different causes as surface conditions of the samples (residual stress, roughness, oxide film) [56],

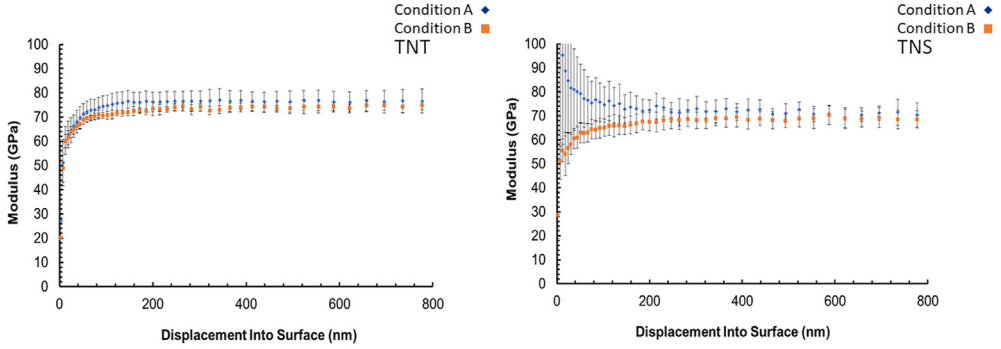

Fig. 10 – Surface elastic moduli of TNT and TNS samples by nanoindentation. The analysis was performed with displacements up to 800 nm on the surface of each material under each condition.

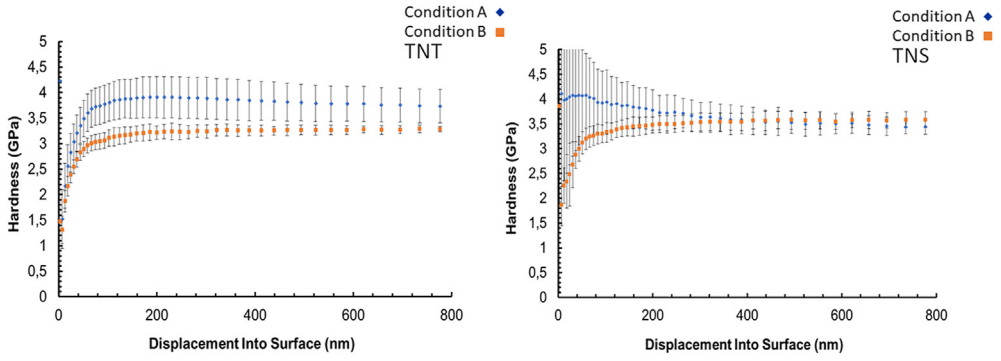

Fig. 11 – Hardness of LSM of the TNT and TNS material by nanoindentation. The analysis was performed with displacements up to 800 nm on the surface of each material under each condition.

Table 4 – Hardness values and elastic modulus obtained by nanoindentation for sintered surfaces and LSM under condition A (LSM A) and condition B (LSM B).

	Elastic modulus E (GPa)			Hardness H (GPa)		
	As sintered	LSM A	LSM B	As sintered	LLSM A	LSM B
TNT	74.0 ± 3.0	76.6 ± 5.5	74.2 ± 2.3	3.3 ± 0.3	3.8 ± 0.4	3.3 ± 0.2
TNS	74.5 ± 2.1	71.4 ± 1.7	68.7 ± 2.1	3.2 ± 0.7	3.5 ± 0.2	3.3 ± 0.2

transitions from an elastic to a fully developed plastic behavior (where only the mean contact pressure represents the hardness) [57] or indentation size effects (ISE) [58].

Table 4 lists the *H* and *E* values averaged over the stable part of the curves (200–800 nm) for the as-sintered and LSM processed materials. In the as-sintered condition, both materials show similar mechanical properties (in terms of *H* and *E*). After LSM, a slight reduction of the elastic modulus is noticed, which is more significant in the TNS alloy. A hardness increase is observed in both materials. These changes could be understood in terms of the extent of the induced martensite transformation. The lower reduction effect in the elastic modulus for the TNT with respect to TNS is explained by the smaller α'' content after LSM. The presence of the harder α'' phase also explains the increased hardness for the two materials, but in this case, no clear correlation is seen with the amount of martensitic transformation. In the same way, the effect of the different laser parameters is not clearly appreciated. Although E values suggest a certain correlation with the scanning speed (a higher E reduction with increasing the scanning speed), deviations are consistent with error estimations. This is not surprising given the modest effect of the variation of scanning speed in the resulting α'' volume fractions, as noted in previous section. Overall, results indicate that LSM processing effectively produces α'' martensitic transformations, leading to a reduction in the elastic modulus of the material and increased hardness. However, its effect is moderate when compared with metallurgical changes caused by mechanical means. This agrees with observations reported by other authors as Fanton et al. [36] which on an equivalent Ti–Nb–Sn alloy obtained an E reduction from 74 to 63 GPa and H increase from 2.5 to 3.1 GPa when cold rolled. With the laser treatment, it was possible to obtain a dense fused layer of the sintered material (as seen in Fig. 3). This dense layer promotes improvement in mechanical properties, such as an increase in hardness and decrease the elastic modulus, by the significant α'' phase formation after LSM, which presents a smaller elastic modulus than the β phase.

This improvement in mechanical properties is also related to the closing open pores. It is known that micropores are formed due to the trapping of gases after the solidification process [59,60]. These formed pores impair the mechanical properties by concentrating the stresses in components under applied load, thus reducing the resistance to fatigue, compression and elongation [61].

4. Conclusion

LSM was used in Ti–35Nb–10Ta (TNT) and Ti–30Nb–4Sn (TNS) applying a specific energy per surface area of 75 J/mm^2 in two treatment conditions: 1000 W at 6.7 mm/s (Condition A) and 1500 W at 10 mm/s (Condition B). The laser treatment improved the surface quality of base sintered samples and produced changes in mechanical properties. The highlighted conclusions of this process are:

- A dense surface layer is obtained which thickness (average 200 μm) depends on the thermal properties of the material and the melt pool dynamics of the laser treatment;
- A dendritic microstructure and homogenous elemental distribution were obtained, despite some micro-segregation effects;
- The base microstructure (β grains with α plate precipitates) changes to a martensitic structure of α'', α and β matrix;
- The mechanical effects (moderate increase in hardness and decrease in E) are more noticeable in the near β TNS alloy. No significant differences were observed in terms of the different process parameters

Declaration of Competing Interest

The authors declare that they have no known competing financial interests or personal relationships that could have appeared to influence the work reported in this paper.

Acknowledgment

This work was supported by the Ministerio Español de Ciencia, Innovación y Universidades, Spain with Grant RTI2018-097810-B-I00, RTI2018-096472-B-I00 and the European Union (EU) through Fondo Europeo de Desarrollo Regional (FEDER), Spain.

REFERENCES

[1] Kuroda D, Niinomi M, Morinaga M, Kato Y, Yashiro T. Design and mechanical properties of new β type titanium alloys for implant materials. Mater Sci Eng A 1998;243(1–2):244–9. https://doi.org/10.1016/s0921-5093(97)00808-3.
[2] Kolli RP, Devaraj A. A review of metastable beta titanium alloys. Metals 2018;8:506. https://doi:10.3390/met8070506.
[3] Niinomi M. Mechanical biocompatibilities of titanium alloys for biomedical applications. J Mech Behav Biomed Mater 2008;1(1):30–42. https://doi:10.1016/j.jmbbm.2007.07.001.
[4] Tane M, Hagihara K, Ueda M, Nakano T, Okuda Y. Elastic-modulus enhancement during room-temperature aging and its suppression in metastable Ti-Nb-Based alloys with low

body-centered cubic phase stability. Acta Mater 2016;102:373–84. https://doi:10.1016/j.actamat.2015.09.030.
[5] Amigó A, Afonso CRM, Amigó V. Effect of Fe addition on microstructure and properties of powder metallurgy Ti35Nb10Ta alloy. Mater Sci Forum 2017:206–11. https://doi:10.4028/www.scientific.net/MSF.899.206.
[6] Kopova I, Stráský J, Harcuba P, Landa M, Janeček M, Bačákova L. Newly developed Ti-Nb-Zr-Ta-Si-Fe biomedical beta titanium alloys with increased strength and enhanced biocompatibility. Mater Sci Eng C 2016;60:230–8. https://doi:10.1016/j.msec.2015.11.043.
[7] Sakaguch N, Niinomi M, Akahori T. Tensile deformation behavior of Ti-Nb-Ta-Zr biomedical alloys. Mater Trans 2004;45(4):1113–9. https://doi:10.2320/matertrans.45.1113.
[8] James WB, H. Corporation. Powder metallurgy methods and applications. In: Samal PK, Newkirk JW, editors. ASM Handbook. Powder Metall. ASM International; 2015. p. 9–19. https://doi:10.31399/asm.hb.v07.a0006022.
[9] Taddei EB, Henriques VAR, Silva CRM, Cairo CAA. Production of new titanium alloy for orthopedic implants. Mater Sci Eng C 2004;2(5):683–7. https://doi:10.1016/j.msec.2004.08.011.
[10] Oksiuta Z, Dabrowski JR. Rotary cold re-pressing and heat treatment of sintered materials from Co-Cr-Mo alloy powder. Powder Metall 2002;45(1):63–6. https://doi:10.1179/003258902225001533.
[11] Salimijazi HR, Mousavi ZA, Golozar MA, Mostaghimi J, Coyle T. Kinetic study of the solid-state transformation of vacuum-plasma-sprayed Ti-6Al-4V alloy. J Therm Spray Technol 2014;23:31–9. Springer, https://doi:10.1007/s11666-013-0025-6.
[12] Liu Y, Yao SW, Ke HB, Liu ZY. Research on surface treatment technologies of Ti6Al4V alloys. In: Appl. Mech. Mater. Trans Tech Publications Ltd.; 2014. p. 569–72. https://doi:10.4028/www.scientific.net/AMM.670-671.569.
[13] Liu X, Chu PK, Ding C. Surface modification of titanium, titanium alloys, and related materials for biomedical applications. Mater Sci Eng Rep 2004;47(3–4):49–121. https://doi:10.1016/j.mser.2004.11.001.
[14] Zambrano JC, Cárcel B, Pereira JC, Amigó V. Recubrimientos laser cladding de TiAl Sobre Ti6Al4V: caracterización tribologica. Rev Latinoam Metal Mater 2016;36. ISSN: 0255-6952:45–53. Available in: http://ve.scielo.org/scielo.php?script=sci_arttext&pid=S025569522016000100007&lng=es&nrm=iso.
[15] Liu W, Liu S, Wang L. Surface modification of biomedical titanium alloy: micromorphology, microstructure evolution and biomedical applications. Coatings 2019;9:249. https://doi:10.3390/coatings9040249.
[16] Fogagnolo JB, Rodrigues AV, Sallica-Leva E, Lima MSF, Caram R. Surface stiffness gradient in Ti parts obtained by laser surface alloying with Cu and Nb. Surf Coat Technol 2016;297:34–42. https://doi:10.1016/j.surfcoat.2016.04.025.
[17] Fogagnolo JB, Rodrigues AV, Lima MSF, Amigó V, Caram R. A novel proposal to manipulate the properties of titanium parts by laser surface alloying. Scr Mater 2013;68:471–4. https://doi:10.1016/j.scriptamat.2012.11.016.
[18] Candel JJ, Amigó V. Recent advances in laser surface treatment of titanium alloys. J Laser Appl 2011;23:022005. https://doi:10.2351/1.3574020.
[19] Zhang F, Qiu Y, Hu T, Clare AT, Li Y, Zhang L-Ch. Microstructures and mechanical behavior of beta-type Ti-25V-15Cr-0.2Si titanium alloy coating by laser cladding. Mater Sci Eng A 2020;796:140063. https://doi:10.1016/j.msea.2020.140063.
[20] El Koumy SR, Barakat ESI, Abdelsalam SI. Hall and porous boundaries effects on peristaltic transport through porous medium of a Maxwell model. Transp Porous Med 2012;94:643–58. https://doi.org/10.1007/s11242-012-0016-y.
[21] Sadaf H, Abdelsalam SI. Adverse effects of a hybrid nanofluid in a wavy non-uniform annulus with convective boundary conditions. RSC Adv 2020;10:15035–43. https://doi.org/10.1039/D0RA01134G.
[22] Bhatti MM, Abdelsalam SI. Thermodynamic entropy of a magnetized Ree-Eyring particle-fluid motion with irreversibility process: a mathematical paradigm. J Appl Math Mech 2020;101:e202000186. https://doi.org/10.1002/zamm.202000186.
[23] Vilar R, Almeida A. Laser surface treatment of biomedical alloys. In: Laser Surf. Modif. Biomater.; 2016. p. 35–75. https://doi:10.1016/B978-0-08-100883-6.00002-2.
[24] Zhang L-Ch, Chen L-Y, Wang L. Surface modification of titanium and titanium alloys: technologies, developments, and future interests. Adv Eng Mater 2019;22:1901258. https://doi:10.1002/adem.201901258.
[25] Eldesoky IM, Abdelsalam SI, El-Askary WA, El-Refaey AM, Ahmed MM. Joint effect of magnetic field and heat transfer on particulate fluid suspension in a catheterized wavy tube. BioNanoScience 2019;9:723–39. https://doi.org/10.1007/s12668-019-00651-x.
[26] Travessa DN, Guedes GVB, de Oliveira AC, Cardoso KR, Roche V, Jorge Jr AM. The effect of surface laser texturing on the corrosion performance of the biocompatible β-Ti12Mo6Zr2Fe alloy. Surf Coat Technol 2021;405:126628. https://doi.org/10.1016/j.surfcoat.2020.126628.
[27] Rakesh KR, Bontha S, Ramesh MR, Das M, Balla VK. Laser surface melting of Mg-Zn-Dy alloy for better wettability and corrosion resistance for biodegradable implant applications. Appl Surf Sci 2019;480:70–82. https://doi.org/10.1016/j.apsusc.2019.02.167.
[28] Luo GX, Wu GQ, Huang Z, Ruan ZJ. Microstructure transformations of laser-surface-melted near-alpha titanium alloy. Mater Charact 2009;60(6):525–9. https://doi.org/10.1016/j.matchar.2008.12.009.
[29] Matsumoto H, Watanabe S, Hanada S. Beta TiNbSn alloys with low Young's modulus and high strength. Mater Trans 2005;46(5):1070–8. https://doi:10.2320/matertrans.46.1070.
[30] Jung TK, Lee HS, Semboshi S, Masahashi N, Abumiya T, Hanada S. A new concept of hip joint stem and its fabrication using metastable TiNbSn alloy. J Alloys Compd 2012:S582–5. https://doi:10.1016/j.jallcom.2011.12.077.
[31] Cai S, Schaffer JE, Ren Y. Deformation of a Ti-Nb alloy containing α-martensite and omega phases. Appl Phys Lett 2015;106:1–6. https://doi:10.1063/1.4916960.
[32] Hanada S, Masahashi N, Jung TK. Effect of stress-induced α″ martensite on Young's modulus of β Ti-33.6Nb-4Sn alloy. Mater Sci Eng A 2013;588:403–10. https://doi:10.1016/j.msea.2013.09.053.
[33] Kharia KK, Rack HJ. Martensitic phase transformations in IMI 550 (Ti-4Al-4Mo-2Sn-0.5 Si). Metall Mater Trans A Phys Metall Mater Sci 2001;32(13):671–9. https://doi:10.1007/s11661-001-1002-0.
[34] D'yakonova NB, Lyasotskii IV, Rodionov YL. Orthorhombic martensite and the ω phase in quenched and deformed titanium alloys with 20-24 at % Nb. Russ Metall 2007;1:51–8. https://doi:10.1134/S0036029507010107.
[35] Zhang T, Fan Q, Ma X, Wang W, Wang K, Shen P, et al. Effect of laser remelting on microstructural evolution and mechanical properties of Ti-35Nb-2Ta-3Zr alloy. Mater Lett 2019;253:310–3. https://doi:10.1016/j.matlet.2019.06.105.
[36] Fanton L, de Lima NB, Encinas ER, Borrás VA, Afonso CRM, Fogagnolo JB. Effects of laser surface melting on crystallographic texture, microstructure, elastic modulus

and hardness of Ti–30Nb–4Sn alloy. Trans Nonferrous Met Soc China 2020;30:392–404. https://doi:10.1016/S1003-6326(20)65221-9.
[37] Tobar MJ, Amado JM, Amigó A, Haro M, Yañez A, Amigó V. Características de la fusión superficial, por láser, de la aleación Ti30Nb4Sn obtenida por pulvimetalurgia. In: Herranz G, Ferrari B, Cabrera JM, editors. VI Congr. Nac. Pulvimetalurgia y I Congr. Iberoam. Pulvimetalurgia; 2017. p. 181–6.
[38] Candel JJ, Amado JM, Amigó V, Tobar MJ. Effects of laser surface melting on Ti–30Nb–2Sn sintered alloy. Adv Eng Mater 2017;19(6):1500640. https://doi:10.1002/adem.201500640.
[39] Eagar TW, Tsai NS. Temperature fields produced by traveling distributed heat sources. Weld Res Suppl 1983;62:346–55.
[40] Kovalev OB, Gusarov AV, Belyaev VV. Morphology of random packing of micro-particles and its effect on the absorption of laser radiation during selective melting of powders. Int J Eng Sci 2020;157:103378. https://doi.org/10.1016/j.ijengsci.2020.103378.
[41] Zhang Y, Liu HS, Jin ZP. Thermodynamic assessment of the Nb-Ti system. Calphad 2001;25:305–17. https://doi:10.1016/S0364-5916(01)00051-7.
[42] Antonova N, Firstov SA, Miracle DB. Investigation of phase equilibria in the Ti-Al-Si-Nb system at low Nb contents. Acta Mater 2003;51:3095–107. https://doi:10.1016/S1359-6454(03)00121-6.
[43] Wei HL, Mukherjee T, Debroy T. Grain growth modeling for additive of nickel based superalloys. Springer; 2016. p. 265–9. https://doi:10.1007/978-3-319-48770-0_39.
[44] Kurz W, Trivedi R. Rapid solidification processing and microstructure formation. Mater Sci Eng A 1994;17:46–51. https://doi.org/10.1016/0921-5093(94)90162-7.
[45] Daloz D, Hecht U, Zollinger J, Combeau H, Hazotte A, Založnik M. Microsegregation, macrosegregation and related phase transformations in TiAl alloys. Intermetallics 2011;19:749–56. https://doi:10.1016/j.intermet.2010.11.013.
[46] Liu G, Li X, Su Y, Liu D, Guo J, Fu H. Microstructure, microsegregation pattern and the formation of B2 phase in directionally solidified Ti-46Al-8Nb alloy. J Alloys Compd 2012;541:275–82. https://doi:10.1016/j.jallcom.2012.07.023.
[47] Abdel-Hady M. Texturing tendency in β-type Ti-alloys. In: Recent Dev. Study Recryst, vol. 201. InTech; 2013. https://doi:10.5772/53588.
[48] Chen W, Chen C, Zi X, Cheng X, Zhang X, Lin YC, et al. Controlling the microstructure and mechanical properties of a metastable β titanium alloy by selective laser melting. Mater Sci Eng A 2018;726:240–50. https://doi:10.1016/j.msea.2018.04.087.
[49] Kim HY, Ikehara Y, Kim JI, Hosoda H, Miyazaki S. Martensitic transformation, shape memory effect and superelasticity of Ti–Nb binary alloys. Acta Mater 2006;54:2419–29. https://doi:10.1016/j.actamat.2006.01.019.
[50] Mantani Y, Tajima M. Phase transformation of quenched α" martensite by aging in Ti–Nb alloys. Mater Sci Eng A 2006;438–440:315–9. https://doi:10.1016/j.msea.2006.02.180.
[51] Ahmed T, Rack HJ. Martensitic transformations in Ti-(16-26 at %) Nb alloys. J Mater Sci 1996;31:4267–76. https://doi:10.1007/BF00356449.
[52] Davis R, Flower HM, West DRF. Martensitic transformations in Ti-Mo alloys. J Mater Sci 1979;14:712–22. https://doi:10.1007/BF00772735.
[53] Haghighi SE, Lu HB, Jian GY, Cao GH, Habibi D, Zhang LC. Effect of α″ martensite on the microstructure and mechanical properties of beta-type Ti-Fe-Ta alloys. Mater Des 2015;76:47–54. https://doi:10.1016/j.matdes.2015.03.028.
[54] Aleixo GT, Afonso CRM, Coelho AA, Caram R. Effects of omega phase on elastic modulus of Ti-Nb alloys as a function of composition and cooling rate. Solid State Phenom 2008;138:393–8. https://doi:10.4028/www.scientific.net/SSP.138.393.
[55] Williams JC, Hickman BS, Marcus HL. The effect of omega phase on the mechanical properties of titanium alloys. Metall Trans 1971;27:1913–9. https://doi:10.1007/BF02913423.
[56] Jia YF, Cui YY, Xuan FZ, Yang F. Comparison between single loading-unloading indentation and continuous stiffness indentation. RSC Adv 2017;7:35655–65. https://doi:10.1039/c7ra06491h.
[57] Yen CY, Jian SR, Tseng YC, Juang JY. The deformation behavior and fracture toughness of single crystal YSZ(111) by indentation. J Alloys Compd 2018;735:2423–7. https://doi:10.1016/j.jallcom.2017.12.022.
[58] Voyiadjis GZ, Peters R. Size effects in nanoindentation: an experimental and analytical study. Acta Mech 2010;211:131–53. https://doi:10.1007/s00707-009-0222-z.
[59] Galarraga H, Lados DA, Dehoff RR, Kirka MM, Nandwana P. Effects of the microstructure and porosity on properties of Ti-6Al-4V ELI alloy fabricated by electron beam melting (EBM). Addit Manuf 2016;10:47–57. https://doi:10.1016/j.addma.2016.02.003.
[60] Aboulkhair NT, Everitt NM, Ashcroft I, Tuck C. Reducing porosity in AlSi10Mg parts processed by selective laser melting. Addit Manuf 2014;1:77–86. https://doi:10.1016/j.addma.2014.08.001.
[61] Weingarten C, Buchbinder D, Pirch N, Meiners W, Wissenbach K, Poprawe R. Formation and reduction of hydrogen porosity during selective laser melting of AlSi10Mg. J Mater Process Technol 2015;221:112–20. https://doi:10.1016/j.jmatprotec.2015.02.013.